NANO LETTERS

pubs.acs.org/NanoLett

Letter

Anisotropic Three-Dimensional Quantum Hall Effect and Magnetotransport in Mesoscopic Weyl Semimetals

Xiao-Xiao Zhang* and Naoto Nagaosa*

Cite This: *Nano Lett.* 2022, 22, 3033−3039

Read Online

ACCESS | Metrics & More | Article Recommendations | Supporting Information

ABSTRACT: Weyl semimetals are emerging to become a new class of quantum-material platform for various novel phenomena. Especially, the Weyl orbit made from surface Fermi arcs and bulk relativistic states is expected to play a key role in magnetotransport, leading even to a three-dimensional quantum Hall effect (QHE). It is experimentally and theoretically important although yet unclear whether it bears essentially the same phenomenon as the conventional two-dimensional QHE. We discover an unconventional fully three-dimensional anisotropy in the quantum transport under a magnetic field. Strong suppression and even disappearance of the QHE occur when the Hall-bar current is rotated away from being transverse to parallel with respect to the Weyl point alignment, which is attributed to a peculiar absence of conventional bulk-boundary correspondence. Besides, transport along the magnetic field can exhibit a remarkable reversal from negative to positive magnetoresistance. These results establish the uniqueness of this QHE system as a novel three-dimensional quantum matter.

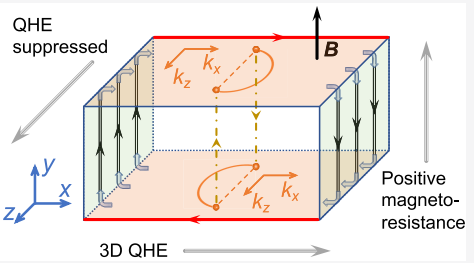

KEYWORDS: *Weyl semimetal, 3D quantum Hall effect, surface state, magnetotransport, 3D anisotropy*

INTRODUCTION

Continuous interest has been sparked by the prediction and experimental realization of three-dimensional (3D) linear band crossings in Weyl semimetal (WSM) systems as a highly nontrivial extension of the two-dimensional (2D) Dirac physics.[1−9] A WSM possesses various intriguing features such as (i) a topologically protected momentum-space monopole structure, (ii) open-arc surface states, (iii) bulk chiral Landau level (LL) formation, (iv) an anomalous Hall effect (AHE), and (v) a chiral magnetic effect and negative magnetoresistance.[10−24] In this new quantum material, the unique 3D closed semiclassical Weyl orbit under magnetic field has been proposed: it consists of a combination of the top and bottom surface Fermi arcs and the bulk chiral LLs, where the latter leads to a real-space vertical trajectory connecting the projection points of a Weyl point (WP) on the orange surfaces in Figure 1a.[25−27] Apart from its detection from quantum phase oscillations, researchers have also envisaged a 3D quantum Hall effect (QHE) based on such an orbit in mesoscopic WSMs.[28] Previous studies have focused on the dependence of magnetic field direction and clarified other possible mechanisms;[29−32] experimental investigation in related materials has also found encouraging evidence of the Weyl orbit.[27,33−38]

Since the QHE is essentially a 2D phenomenon, it is an intriguing question whether the nature of this new QHE remains the same as in two dimensions.[39−41] Surprisingly, dissimilar to what one would expect for a QHE-like phenomenon, there hides essential and intrinsic anisotropy in the magnetotransport, which can in general affect and even diminish the QHE. The clear QHE features when current flows transversely to the momentum-space WP alignment will be strongly suppressed as

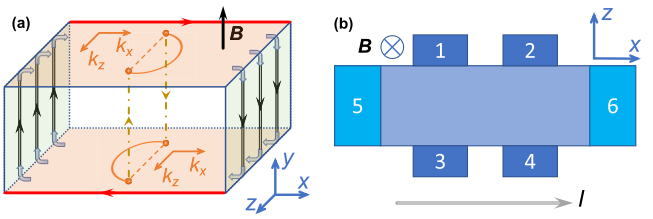

Figure 1. (a) 3D bulk WSM system under a magnetic field. The orange top and bottom surfaces at $y = \pm L_y/2$ are always connected by the green side surfaces at $x = \pm L_x/2$ due to the topological arc circulating states. The red arc LL edge states lead to the robust QHE. To illustrate the Weyl orbit, we use a mixed representation: on the top and bottom surfaces we indicate in **k**-space the Fermi arcs connecting two WPs along k_z; the brown dot-dashed lines along the real y-axis indicate the bulk chiral LLs. Note that such chiral LLs exist everywhere in the **r**-space. (b) Six-terminal Hall-bar system under magnetic field $\mathbf{B} = B\hat{y}$. Leads 1, 2, 3, and 4 measure the voltage while a current flows through leads 5 and 6. The two-terminal case has leads 5 and 6 only. The axes exemplify the zx-geometry with the QHE signal.

Received: January 24, 2022
Revised: March 8, 2022
Published: March 25, 2022

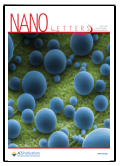

https://doi.org/10.1021/acs.nanolett.2c00296
Nano Lett. 2022, 22, 3033−3039

Table 1. Summary of the Magnetotransport along Three Orthogonal Directions[a]

$\mathbf{B} = B\hat{y}$	current direction i		
	x (QHE)**	y*	z
major contribution	diagonal edge states from arc LLs	arc channels + bulk chiral LLs	surface hybridized states
two-terminal conductance $G_{ii}/\frac{e^2}{h}$	$G_{xx} = n$	$G_{yy}(W-)$	$G_{zz}(W-)$
six-terminal resistance $R_{ji}/\frac{h}{e^2}$	$R_{xx} = 0$ $\tilde{R}_{xx} = R_{xx} = R_{yx} = \frac{1}{n}$	$R_{yy}(B\mp) \ll 1$ $\tilde{R}_{yy} \approx G_{yy}^{-1}$	$R_{zz}(W+) \neq 0$ $\tilde{R}_{zz} \neq R_{xz} \neq \frac{1}{n}$

[a]Current directions $i = x, y, z$ in the WSM with WPs along the k_z-axis. Number of * indicates the stability against disorder: $i = y$ exhibits a moderate stability weaker than the QHE when $i = x$ but stronger than the vulnerable $i = z$ case. Major transport contributing channels are listed. n for quantized integer in the QHE. $G_{yy,zz}(W{=}0)$ is quantized to the number of contributing channels not related to the QHE. Besides Hall and longitudinal resistances R_{ji}, one has another resistance $\tilde{R}_{ii}$ between two current leads in the six-terminal measurement. $W+$ ($W-$) means increasing (decreasing) as the disorder strength W increases. Small R_{yy} originates from the separation in both $\mathbf{k}$- and $\mathbf{r}$-space of the counterpropagating conducting channels. $B\mp$ signifies the reversal from negative to positive magnetoresistance.

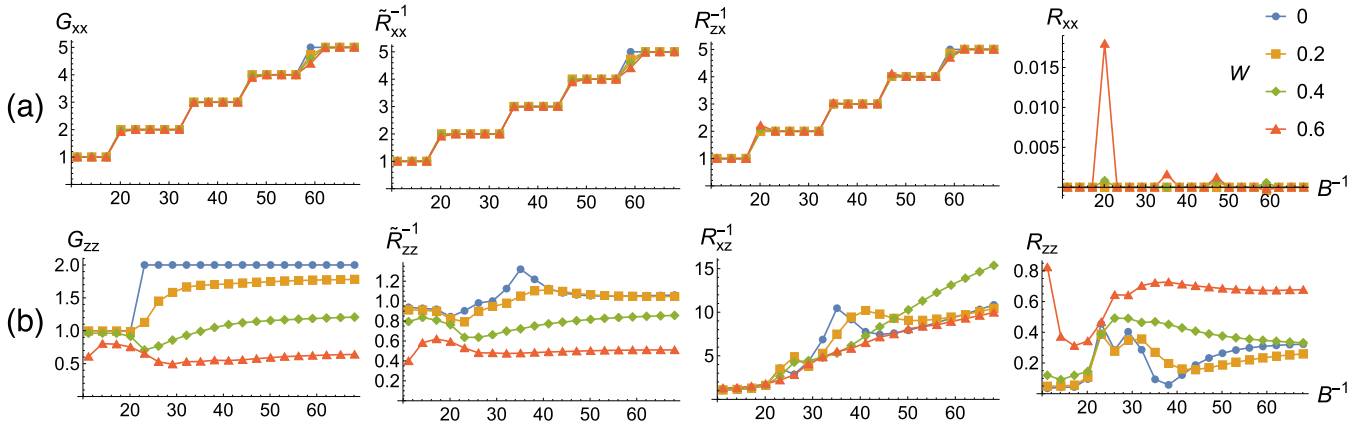

Figure 2. Hall and longitudinal transport responses, including the two-terminal conductance G_{ii} and six-terminal resistances for two orthogonal probing geometries, i.e., current flowing along (a) $i = x$ and (b) $i = z$. R_{ii},R_{ji} are the longitudinal and Hall resistances; $\tilde{R}_{ii}$ is the resistance between current leads. Colors denote the disorder strength W. System size $L_x = L_z = 37$, $L_y = 28$. Parameters throughout this paper are $A = 1$, $M = 0.15$, $D_x = 0.06$, $D_y = 0.03$, $D_z = 0.09$, and $k_w = \pi/2$, and we set $e^2/h = 1$.

one deviates from this probing geometry. In the orthogonal setting with current parallel to the WP alignment, the system does not show a QHE and is the most susceptible to disorder. The origin can be traced back to an unexpected absence of bulk-boundary correspondence (BBC), and all three directions play different roles: arc surface states from the quantum anomalous Hall effect (QAHE) edge states are defined on momentum slices only between the WPs, and the role of green side surfaces is distinct from the front and back surfaces in Figure 1a. Besides revealing the fundamental difference between the conventional QHE and this 3D WSM QHE, transport along the applied magnetic field shows a remarkable reversal of the well-known negative magnetoresistance due to chiral anomaly, which is attributed to a nontrivial competition between surface and bulk contributions. To summarize, there are three directions, i.e., those of the applied magnetic field, the alignment of WPs, and that perpendicular to the previous two; the system exhibits an overlooked but essential anisotropy with respect to the transport direction relative to these three (Table 1).

RESULTS

We consider the following minimal two-band model with two WPs $(0, 0, \pm k_w)$ located on the k_z-axis and the Fermi energy $\varepsilon_F = 2D_z(1 - \cos k_w)$ at the WPs

$$H(\mathbf{k}) = \sum_{i=x,y,z} 2D_i(1 - \cos k_i)\sigma_0 + A(\sin k_x\sigma_x + \sin k_y\sigma_y) + 2M\left[(1 - \cos k_w) - \sum_{i=x,y,z}(1 - \cos k_i)\right]\sigma_z \quad (1)$$

where we include mutually unequal $D_{x,y,z}$ for realistic anisotropy giving rise to curved Fermi arcs and a nonvanishing response in every direction. As illustrated in Figure 1b, we use two-terminal and six-terminal Hall-bar probing geometries, where WSM current leads cover two surfaces and metallic voltage leads have limited size.[42,43] Unless otherwise stated, we apply a magnetic field $\mathbf{B} = B\hat{y}$ via the Peierls substitution $\mathbf{k} \to \mathbf{k} + e\mathbf{A}$ and average over an onsite disorder uniformly distributed in $[-W/2, W/2]$. For a current flowing along the i-axis, apart from the two-terminal conductance G_{ii}, the six-terminal Hall bar measures either the Hall ($j \neq i$) or longitudinal ($j = i$) resistance R_{ji}. Another $\tilde{R}_{ii}$ between leads 5 and 6 would give the identical Hall resistance R_{ji} if the BBC in the conventional QHE was preserved, i.e., contributed by the quantized contact resistance from edge states as G_{ii}. To calculate the transmission probability in the Landauer−Büttiker formula, we adopt the wave function scattering matrix approach equivalent to the nonequilibrium Green function.[44−46]

Suppression of the QHE in an Orthogonal Geometry. In Figure 2, we show the conductance and resistance for two

https://doi.org/10.1021/acs.nanolett.2c00296
Nano Lett. 2022, 22, 3033−3039

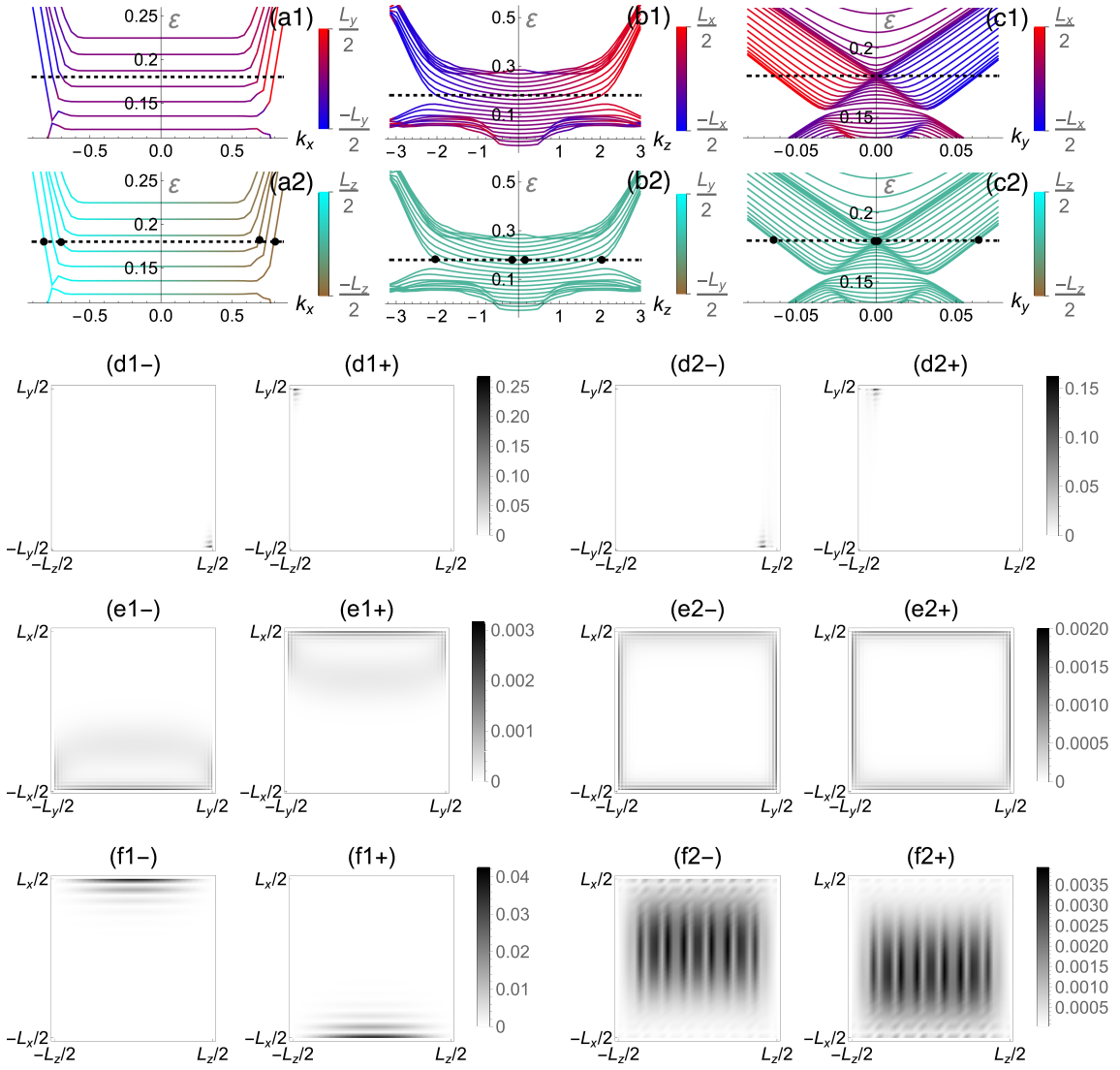

Figure 3. (a–c) Low-energy bands under a magnetic field with (a) periodic x-axis and $L_y = L_z = 60$, $B = 0.025$, (b) periodic z-axis and $L_x = L_y = 90$, $B = 0.025$, (c) periodic y-axis and $L_x = L_z = 30$, $B = 0.1$. The main features are stable against large enough system sizes. The Fermi energy $\varepsilon_F = 0.18$ is indicated by the dashed line. Color scales indicate the real-space position expectation value $\langle y\rangle$, $\langle z\rangle$, $\langle x\rangle$, $\langle y\rangle$, $\langle x\rangle$, and $\langle z\rangle$, respectively for (a1), (a2), (b1), (b2), (c1), and (c2) of the corresponding wave function. Note that $\langle y\rangle$ and $\langle z\rangle$ are mostly close to zero in (b2) and (c2). (d–f) Wave function probability distribution in three cross sections (d) yz, (e) yx, and (f) zx, respectively, corresponding to (a), (b), and (c). For (d), wave functions from two representative bands crossing the Fermi level in (a), typically with (d1) largest or (d2) smallest k_F along k_x as indicated by black dots in (a2), are shown; within (d1), for instance, (d1±) shows the state at positive/negative $k_x = \pm k_F$ of that particular band. (e, f), labeled and sorted in the similar manner, are from the black dots in (b2) and (c2).

orthogonal probing geometries. While the zx-geometry (current along x and voltage leads extend along z) exhibits clear and consistent QHE features robust against disorder,[28,29] the xz-geometry sees entirely distinct behavior. (i) The quantized plateaus disappear in any of G_{zz}, $\tilde{R}_{zz}$, and R_{xz} except for G_{zz} without disorder. (ii) The vanishing longitudinal resistance R_{zz} becomes finite and overall increases with disorder strength in a conventional manner. (iii) The stability against disorder in each signal largely reduces to a minimal level. This indicates that the conducting channels contributing to the transport along two orthogonal directions bear some fundamental difference. Note that this does not contradict the Onsager reciprocity discussed in the Supporting Information (SI Section I).

In fact, without disorder one can visualize the conducting channels thanks to the conserved momentum along the respective current direction. Figure 3 shows the relevant band structure and the corresponding representative cross-sectional wave function probability distribution. In Figure 3a, the projection of both WPs coincide at $k_x = 0$. The formation of LLs in a range across ε_F signifies their origin from the surface Fermi arcs, since the bulk density of states vanishes at ε_F. Then the upward-bending edge of these LLs exactly serves as the red diagonal QHE edge states in Figure 1a under protection from backscattering, which is also readily seen in Figure 3d. In Figure 3b, two WPs at $k_z = \pm\pi/2$ remain separated and are connected by the arc states discretized by finite $L_{x,y}$. Figure 3e1 with large k_F exhibits counterpropagating D-shaped wave functions connecting the top and bottom via the side surface and the bulk, whose semiclassical trajectory has previously been noticed.[29] In Figure 3e2 with small k_F, the top and bottom surfaces and two side surfaces are almost fully connected. In fact, as one plots the conducting wave functions with decreasing k_F, Figure 3e1

https://doi.org/10.1021/acs.nanolett.2c00296
Nano Lett. 2022, 22, 3033−3039

gradually deforms into Figure 3e2. Most importantly, there is no LL formation along k_z, which dictates the disappearance of the QHE together with related features. Large system sizes can at most give few fragile quasiplateaus well below the accuracy and robustness of the QHE (SI Section II). It partially results from the conventional mesoscopic channel quantization as $G_{zz}(W{=}0)$ and may grow in large samples due to denser discretization. The results are summarized in Table 1. See also SI Section I for the complete resistance tensor. Transport along the magnetic field direction $\hat{y}$ in relation to Figure 3c,f will be described later.

Surface theory can help gain further insights.[28,47−49] For the top and bottom $y = \pm L_y/2$ surfaces around $k_x = 0$, we obtain the effective Hamiltonian (SI Section III)

$$h_{\pm}(k_x, k_z) = \varepsilon_0 \pm v' k_x + D'_x k_x^2 - 2D'_z \cos k_z \qquad (2)$$

for k_z between WPs, where $\varepsilon_0 = 2D_z - 2D_y \cos k_w$, $v' = A\sqrt{M^2 - D_y^2}/M$, and $D'_x = D_x - D_y$, $D'_z = D_z - D_y$. The top and bottom Fermi arcs are respectively in the $k_x > 0$ and $k_x < 0$ regions due to positive D'_z. Considering transport along the x-axis, gauge choice $\mathbf{A} = Bz\hat{x}$ and conserved k_x is able to form LLs from essentially the same quasi-1D z-axis cosine gas. Semiclassically, LL states originate from electrons traversing the Weyl orbit previously described with Figure 1a, which consists of arc trajectories connected by bulk chiral LLs. The metallic $\pm L_x/2$ green side surfaces in Figure 1a, which host QAHE circulating states and disperses along y,z-directions, are merged in the current leads. In fact, around the $\pm L_y/2$ surface, arc LL bands bent upward in Figure 3a near the $\mp L_z/2$ edge will just become the $\pm\hat{x}$-propagating red diagonal edge channel in Figure 1a, because of the correspondence between k_x and the guiding center along the z-axis. Figure 3 parts d1 and d2 clearly show such diagonal edge states in the yz-plane. This means that the $h_{\pm}$ contributions to edge LL formation are largely separated in both k_x and real z and do not directly interfere.

However, for transport along the z-axis with gauge choice $\mathbf{A} = -Bx\hat{z}$ and conserved k_z, the top and bottom quasi-1D x-axis gases are not "decoupled" in the previous simple manner. Required by the measurement geometry, the nontrivial green side surfaces in Figure 1a are always present and host similar states as eq 2; their highly nonlocal QAHE circulating states naturally extend into the top and bottom surfaces and play in part the role of connecting states from $h_{\pm}$ under a magnetic field. Therefore, a magnetic arc state at ε_F lives on *both* top and bottom surfaces and exhibits $\langle y\rangle \sim 0$ in Figure 3b2 and possesses a much weaker $\langle x\rangle$-asymmetry in Figure 3b1 than in Figure 3a2. These are readily visualized within the yx-plane in Figure 3e as previously noted. Indicated by these results, the circulating or top-bottom inseparable nature forces hybridization with the bulk and especially metallic side surfaces and generates dispersiveness in Figure 3b; there is thus no flat bulk gap essential to the QHE but hybridized states that allow for scattering. Note that the metallicity of the side surface, e.g., its z-axis dispersion, is indispensable to the 3D QHE as it generates the curved Fermi arcs. Fundamentally, such contrasting behavior between two geometries is the consequence of the WSM topology choosing a direction: WPs are aligned along the k_z-axis. Phenomena possibly related to this have been noticed in the second-harmonic generation and arc optical conductivity.[50,51]

Rotating the System with Respect to the *y*-Axis. In realistic WSM experiments, alignment of WPs as generic band crossings could easily be oblique to the natural crystallographic growth geometry and also the Hall bar, e.g., due to hoppings beyond the nearest neighbor. To address this, we consider a rotation with respect to $\hat{y}$ of the Hall-bar system by a commensurate angle $\theta = \arctan(m_x, m_z)$: the new supercell includes m_i cells along the i-axis for $i = x, z$ (see SI Figure S4). Accordingly, we rotate the gauge $\mathbf{A}(\theta)$ together (SI Section IV), denote the rotated x, z-axes as X, Z, and keep the current flowing along X. When $\theta = 0, \pi/2$, it reproduces the foregoing zx- or xz-geometry. As shown in Figure 4 and additional cases in SI

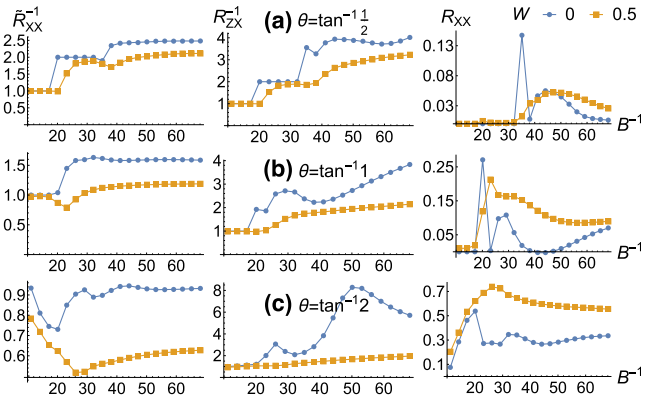

Figure 4. Hall and longitudinal resistances $\tilde{R}_{ii}$, R_{ji}, and R_{ii} for the six-terminal measurement. The current direction $i = X$ (together with the orthogonal $j = Z$ direction) of the Hall bar is rotated with respect to $\hat{y}$ from the original x-axis by a commensurate angle θ. System size $L_y = 24$ and $L_{X,Z}$ use the corresponding commensurate length closest to 38 in three rotation angles (a, b, c) in ascending order. Colors denote the disorder strength W.

Section II, the transport responses exhibit a significant anisotropy. (i) Higher QHE plateaus start to disappear as θ increases from 0. (ii) Beyond $\pi/4$, basically no plateaus can survive. (iii) The remaining plateaus and longitudinal resistances are much more susceptible to the same level of disorder than the zx-geometry in Figure 2a. Even in Figure 4b the first plateau with disorder actually suffers a huge 2% deviation from perfect quantization, compared with 10^{-13} accuracy in Figure 2a. Note also that in the conventional QHE, e.g., a square-lattice electron gas, none of these features are present and the plateaus are always robust against such rotation although the system itself only possesses a C_4 rotation symmetry (SI Section II).

This anisotropy or strong θ-dependence displays a crossover behavior between the two previous cases. With an oblique $\theta > 0$, transport along X is no longer contributed solely by the well-defined arc LL edge states; instead, there always exists a finite projection in the z-direction transport, which is based on the foregoing surface hybridized states without LL formation. As θ increases, the z-axis backscattering affects more and more the X-axis current, which does not play a role when $\theta = 0$. Therefore, the QHE will deteriorate to some extent with any finite θ because the formation and robustness of plateaus and the vanishing longitudinal resistance indispensably rely on an exclusive LL edge-state transport.

Absence of Conventional Bulk-Boundary Correspondence. An important aspect of the conventional QHE consists in the BBC, where the number of conducting edge channels can be uniquely determined by the bulk topological Chern number.[52,53] Combining the foregoing physical picture and concrete transport responses, we conclude that the QHE in a 3D WSM does not possess an usual BBC. First, a direct consequence of

https://doi.org/10.1021/acs.nanolett.2c00296
Nano Lett. 2022, 22, 3033−3039

BBC in the conventional QHE is the aforementioned identity $\tilde{R}_{ii} = R_{ji}$ when directions i, j with $i \neq j$ are perpendicular to magnetic field, which is violated as long as $i \neq x$ or $\theta \neq 0$ as shown in Figures 2 and 4. Second, the QHE hereof largely relies on the presence of surface arc states under magnetic field, where ϵ_F pinpointed at the WP crosses arc LLs only in Figure 3a and bulk states participate in a supporting way. This renders it physically infeasible to define a *bulk* topological invariant. Importantly, the present phenomenon is distinct from the earlier 3D QHE scheme characterized by Chern numbers defined for three orthogonal planes, which is purely a bulk magnetic band property caused by the charge-density-wave gap etc.[54−59] Third, to reassure this viewpoint, one can actually calculate the conductivity σ_{zx} from the lattice model via the Kubo−Bustin formalism with the kernel polynomial method, where operator evaluation is restricted deep *inside* the bulk.[60−62] While it fails to display the present QHE, the same calculation well shows both the conventional QHE in a 2D electron gas and the expected AHE σ_{xy} proportional to $|2k_w|$ in this WSM system (SI Section V). This is simply because the latter two cases bear the topological BBC.

Transport Parallel to the Magnetic Field. The remaining y-axis magnetotransport also has notable features. This configuration is relevant to the negative magnetoresistance due to chiral anomaly in a WSM, where chiral pumping via bulk chiral LLs between WPs is at work.[10−12] As shown in Figure 5,

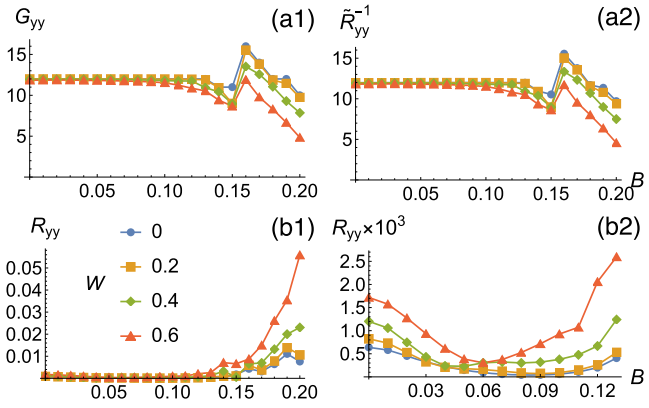

Figure 5. Magnetotransport parallel to the magnetic field along the y-axis. (a1, a2) Conductance G_{yy} and resistance $\tilde{R}_{yy}$. (b2) zooms in the low-field region of the longitudinal resistance R_{yy} in (b1) where the reversal from negative to positive magnetoresistance happens. System size $L_x = L_z = 30$, $L_y = 100$.

G_{yy}, $\tilde{R}_{yy}$ consistently remain nearly constant until a large field destroys the contributing QAHE accumulated between WPs. Before that, the robustness against disorder is intermediate between the previous two orthogonal zx- and xz-geometries; relatedly, the longitudinal $R_{yy} \ll 1$ but is not vanishing and $\tilde{R}_{yy}$ approximately follows G_{yy}^{-1}, as indicated in Table 1. This intermediate stability results from a combination of **k**- and **r**-space separation unique to this transport direction. The relevant conducting channels along the y-axis include two parts in Figure 3c1. (i) Red and blue QAHE edge states near the $x = \pm L_x/2$ side surfaces are spatially separated. (ii) Two sets of counter-propagating purple bulk chiral LLs cross at $k_y = 0$ where the projection of two WPs coincides; they are distributed inside the system bulk and also near the side surface. Figure 3 parts f1 and f2, respectively, show the probability distribution of these two types of states in the zx-plane.

Intriguingly in Figure 5b1 and the magnified Figure 5b2, the negative magnetoresistance is very weak and holds only up to a medium field strength, as disorder can strongly suppress and reverse it to positive magnetoresistance. The reversal point moves to smaller field strength with either larger W or L_y. Note that this is entirely absent in the other geometry when B and current I both are along the z-axis, i.e., parallel to the WP alignment, where negative magnetoresistance persists all along (SI Section I). This robust negative magnetoresistance means that, although the **k**-space separated bulk chiral LLs are subject to large-momentum-transfer disorder scattering, the increasing number of these chiral channels with larger B guarantees it. Physically, the main difference in Figure 5b from the $\mathbf{B}\|I\|\hat{z}$ situation is the contribution from the aforementioned nontrivial green side surfaces in Figure 1a that host topological states conducting along the y-axis. These dispersive surface states can themselves be backscattered and especially to the counter-propagating chiral LLs also present at the side surfaces, which is made easier and more frequent by the denser guiding center lattice at larger B: the side-surface contribution is purely positive magnetoresistance. Remarkably in this competition, eventually the surface backscattering prevails and dominantly contributes to the longitudinal resistance R_{yy}. In a 3D bulk sample with L_y comparable to or even larger than the mean free path, such a positive magnetoresistance will naturally be expected to occur and it reveals the crucial but overlooked surface magnetotransport contribution in a WSM.

DISCUSSION

We examine the 3D QHE and magnetotransport in WSM systems from the experimentally most relevant viewpoint of a Hall-bar measurement. Our findings establish the system as a novel quantum state of matter of highly nontrivial fully 3D anisotropy and reveal the peculiar surface-bulk-hybrid nature of magnetotransport with no conventional counterpart, e.g., in the ordinary 2D QHE. It is expected to provide immediate and key insights to the experimental investigation. Although we mainly concern the case with one single pair of WPs as the physically most clarifying situation, the general consideration can be readily extended to more complicated cases with multiple pairs of WPs, regardless of a magnetic or nonmagnetic WSM (SI Section VI).

Among experimental reports of quantized transport in the closely related Dirac semimetal Cd_3As_2, a few provide supportive evidence of the role of Weyl orbit via thickness modulation and dual-gate modulation between top and bottom surfaces.[27,36,38] In the experiment with a nanobelt grown by chemical vapor deposition, current along the in-plane $[1\bar{1}0]$ direction flows through the sample with surfaces normal to the magnetic field in the $[112]$ direction.[36] One can identify them respectively as $\hat{x}$ and $\hat{y}$ directions in our discussion. The Dirac points along the $[001]$ direction (oblique but inside the yz-plane) lead to pairs of Fermi arcs along the z-axis on the top and bottom surfaces in a similar manner as in Figure 1a. The front and back surfaces can also host surface states propagating along the x-axis but do not affect the red diagonal edge states in Figure 1a. Hence it is akin to the zx-geometry with the QHE as discussed. In the other thin-film experiment using solid-phase epitaxy, the in-plane current direction is presumed to include the $[1\bar{1}0]$ and $[11\bar{1}]$ directions due to the presence of two possible domains.[38] Therefore, this situation corresponds to the rotated case effectively and is still possible to exhibit lower quasiplateaus in the mesoscopic transport as we discussed. Indeed, the quantization bears a much

https://doi.org/10.1021/acs.nanolett.2c00296
Nano Lett. 2022, 22, 3033−3039

more extended and robust appearance and the longitudinal resistivity is even closer to zero in the former nanobelt experiment,[36] which is consistent with our study. Further experiments in especially WSMs under various geometries we proposed will certainly be helpful to firmly observing the intriguing 3D anisotropic effects.

■ ASSOCIATED CONTENT

Supporting Information

The Supporting Information is available free of charge at https://pubs.acs.org/doi/10.1021/acs.nanolett.2c00296.

Other geometries and additional data sets, details of model analysis, conductivity calculation, and discussion of multiple pairs of Weyl points (PDF)

■ AUTHOR INFORMATION

Corresponding Authors

Xiao-Xiao Zhang − *RIKEN Center for Emergent Matter Science (CEMS), Wako, Saitama 351-0198, Japan;* orcid.org/0000-0003-3142-9232; Email: xiaoxiao.zhang@riken.jp

Naoto Nagaosa − *Department of Applied Physics, University of Tokyo, Tokyo 113-8656, Japan; RIKEN Center for Emergent Matter Science (CEMS), Wako, Saitama 351-0198, Japan;* Email: nagaosa@ap.t.u-tokyo.ac.jp

Complete contact information is available at: https://pubs.acs.org/10.1021/acs.nanolett.2c00296

Notes

The authors declare no competing financial interest.

■ ACKNOWLEDGMENTS

X.-X.Z. is thankful for the helpful discussion with H. Li, M. Uchida, P. Perez-Piskunow, C. Zhang, and Y. Tokura and also for the computation facility coordinated by H. Isobe. This work was supported by JSPS KAKENHI (No. 18H03676) and JST CREST (Nos. JPMJCR1874 & JPMJCR16F1). X.-X.Z was partially supported by the RIKEN Special Postdoctoral Researcher Program.

■ REFERENCES

(1) Volovik, G. E. Linear momentum in ferromagnets. *J. Phys. C: Solid State Phys.* **1987**, *20*, L83.

(2) Murakami, S. Phase transition between the quantum spin Hall and insulator phases in 3D: emergence of a topological gapless phase. *New J. Phys.* **2007**, *9*, 356.

(3) Wan, X.; Turner, A. M.; Vishwanath, A.; Savrasov, S. Y. Topological semimetal and fermi-arc surface states in the electronic structure of pyrochlore iridates. *Phys. Rev. B* **2011**, *83*, 205101.

(4) Burkov, A. A.; Balents, L. Weyl semimetal in a topological insulator multilayer. *Phys. Rev. Lett.* **2011**, *107*, 127205.

(5) Xu, G.; Weng, H.; Wang, Z.; Dai, X.; Fang, Z. Chern semimetal and the quantized anomalous Hall effect in $HgCr_2Se_4$. *Phys. Rev. Lett.* **2011**, *107*, 186806.

(6) Lv, B. Q.; Weng, H. M.; Fu, B. B.; Wang, X. P.; Miao, H.; Ma, J.; Richard, P.; Huang, X. C.; Zhao, L. X.; Chen, G. F.; Fang, Z.; Dai, X.; Qian, T.; Ding, H. Experimental discovery of Weyl semimetal TaAs. *Phys. Rev. X* **2015**, *5*, 031013.

(7) Xu, S.-Y.; Belopolski, I.; Alidoust, N.; Neupane, M.; Bian, G.; Zhang, C.; Sankar, R.; Chang, G.; Yuan, Z.; Lee, C.-C.; Huang, S.-M.; Zheng, H.; Ma, J.; Sanchez, D. S.; Wang, B.; Bansil, A.; Chou, F.; Shibayev, P. P.; Lin, H.; Jia, S.; Hasan, M. Z. Discovery of a Weyl fermion semimetal and topological fermi arcs. *Science* **2015**, *349*, 613−617.

(8) Yang, L. X.; Liu, Z. K.; Sun, Y.; Peng, H.; Yang, H. F.; Zhang, T.; Zhou, B.; Zhang, Y.; Guo, Y. F.; Rahn, M.; Prabhakaran, D.; Hussain, Z.; Mo, S.-K.; Felser, C.; Yan, B.; Chen, Y. L. Weyl semimetal phase in the non-centrosymmetric compound TaAs. *Nat. Phys.* **2015**, *11*, 728−732.

(9) Lv, B. Q.; Xu, N.; Weng, H. M.; Ma, J. Z.; Richard, P.; Huang, X. C.; Zhao, L. X.; Chen, G. F.; Matt, C. E.; Bisti, F.; Strocov, V. N.; Mesot, J.; Fang, Z.; Dai, X.; Qian, T.; Shi, M.; Ding, H. Observation of Weyl nodes in TaAs. *Nat. Phys.* **2015**, *11*, 724−727.

(10) Nielsen, H.; Ninomiya, M. The adler-bell-jackiw anomaly and Weyl fermions in a crystal. *Phys. Lett. B* **1983**, *130*, 389−396.

(11) Son, D. T.; Spivak, B. Z. Chiral anomaly and classical negative magnetoresistance of Weyl metals. *Phys. Rev. B* **2013**, *88*, 104412.

(12) Burkov, A. Chiral anomaly and diffusive magnetotransport in Weyl metals. *Phys. Rev. Lett.* **2014**, *113*, 247203.

(13) Li, Q.; Kharzeev, D. E.; Zhang, C.; Huang, Y.; Pletikosić, I.; Fedorov, A. V.; Zhong, R. D.; Schneeloch, J. A.; Gu, G. D.; Valla, T. Chiral magnetic effect in $ZrTe_5$. *Nat. Phys.* **2016**, *12*, 550−554.

(14) Xiong, J.; Kushwaha, S. K.; Liang, T.; Krizan, J. W.; Hirschberger, M.; Wang, W.; Cava, R. J.; Ong, N. P. Evidence for the chiral anomaly in the Dirac semimetal Na_3Bi. *Science* **2015**, *350*, 413−416.

(15) Shekhar, C.; Nayak, A. K.; Sun, Y.; Schmidt, M.; Nicklas, M.; Leermakers, I.; Zeitler, U.; Skourski, Y.; Wosnitza, J.; Liu, Z.; Chen, Y.; Schnelle, W.; Borrmann, H.; Grin, Y.; Felser, C.; Yan, B. Extremely large magnetoresistance and ultrahigh mobility in the topological Weyl semimetal candidate NbP. *Nat. Phys.* **2015**, *11*, 645−649.

(16) Liang, T.; Lin, J.; Gibson, Q.; Kushwaha, S.; Liu, M.; Wang, W.; Xiong, H.; Sobota, J. A.; Hashimoto, M.; Kirchmann, P. S.; Shen, Z.-X.; Cava, R. J.; Ong, N. P. Anomalous Hall effect in $ZrTe_5$. *Nat. Phys.* **2018**, *14*, 451−455.

(17) Zhang, C.; Ni, Z.; Zhang, J.; Yuan, X.; Liu, Y.; Zou, Y.; Liao, Z.; Du, Y.; Narayan, A.; Zhang, H.; Gu, T.; Zhu, X.; Pi, L.; Sanvito, S.; Han, X.; Zou, J.; Shi, Y.; Wan, X.; Savrasov, S. Y.; Xiu, F. Ultrahigh conductivity in Weyl semimetal NbAs nanobelts. *Nat. Mater.* **2019**, *18*, 482−488.

(18) Volovik, G. E. *The Universe in a Helium Droplet (International Series of Monographs on Physics)*, 1st ed.; Oxford University Press: Oxford, 2009.

(19) Burkov, A. A. Topological semimetals. *Nat. Mater.* **2016**, *15*, 1145−1148.

(20) Yan, B.; Felser, C. Topological materials: Weyl semimetals. *Annual Review of Condensed Matter Physics* **2017**, *8*, 337−354.

(21) Burkov, A. Weyl metals. *Annual Review of Condensed Matter Physics* **2018**, *9*, 359−378.

(22) Armitage, N. P.; Mele, E. J.; Vishwanath, A. Weyl and Dirac semimetals in three dimensional solids. *Rev. Mod. Phys.* **2018**, *90*, 015001.

(23) Nagaosa, N.; Morimoto, T.; Tokura, Y. Transport, magnetic and optical properties of Weyl materials. *Nature Reviews Materials* **2020**, *5*, 621−636.

(24) Lv, B.; Qian, T.; Ding, H. Experimental perspective on three-dimensional topological semimetals. *Rev. Mod. Phys.* **2021**, *93*, 025002.

(25) Potter, A. C.; Kimchi, I.; Vishwanath, A. Quantum oscillations from surface fermi arcs in Weyl and Dirac semimetals. *Nat. Commun.* **2014**, *5*, 5161.

(26) Zhang, Y.; Bulmash, D.; Hosur, P.; Potter, A. C.; Vishwanath, A. Quantum oscillations from generic surface fermi arcs and bulk chiral modes in Weyl semimetals. *Sci. Rep.* **2016**, *6*, 23741.

(27) Zhang, C.; Zhang, Y.; Lu, H.-Z.; Xie, X. C.; Xiu, F. Cycling fermi arc electrons with Weyl orbits. *Nat. Rev. Phys.* **2021**, *3*, 660−670.

(28) Wang, C.; Sun, H.-P.; Lu, H.-Z.; Xie, X. 3D quantum Hall effect of fermi arcs in topological semimetals. *Phys. Rev. Lett.* **2017**, *119*, 136806.

(29) Li, H.; Liu, H.; Jiang, H.; Xie, X. 3D quantum Hall effect and a global picture of edge states in Weyl semimetals. *Phys. Rev. Lett.* **2020**, *125*, 036602.

(30) Chen, R.; Liu, T.; Wang, C.; Lu, H.-Z.; Xie, X. Field-tunable one-sided higher-order topological hinge states in Dirac semimetals. *Phys. Rev. Lett.* **2021**, *127*, 066801.

(31) Chen, R.; Wang, C. M.; Liu, T.; Lu, H.-Z.; Xie, X. C. Quantum Hall effect originated from helical edge states in Cd_3As_2. *Physical Review Research* **2021**, *3*, 033227.
(32) Chang, M.; Geng, H.; Sheng, L.; Xing, D. Y. Three-dimensional quantum Hall effect in Weyl semimetals. *Phys. Rev. B* **2021**, *103*, 245434.
(33) Zhang, C.; Narayan, A.; Lu, S.; Zhang, J.; Zhang, H.; Ni, Z.; Yuan, X.; Liu, Y.; Park, J.-H.; Zhang, E.; Wang, W.; Liu, S.; Cheng, L.; Pi, L.; Sheng, Z.; Sanvito, S.; Xiu, F. Evolution of Weyl orbit and quantum Hall effect in Dirac semimetal Cd_3As_2. *Nat. Commun.* **2017**, *8*, 1272.
(34) Uchida, M.; Nakazawa, Y.; Nishihaya, S.; Akiba, K.; Kriener, M.; Kozuka, Y.; Miyake, A.; Taguchi, Y.; Tokunaga, M.; Nagaosa, N.; Tokura, Y.; Kawasaki, M. Quantum Hall states observed in thin films of Dirac semimetal Cd_3As_2. *Nat. Commun.* **2017**, *8*, 2274.
(35) Schumann, T.; Galletti, L.; Kealhofer, D.; Kim, H.; Goyal, M.; Stemmer, S. Observation of the quantum Hall effect in confined films of the three-dimensional Dirac semimetal Cd_3As_2. *Phys. Rev. Lett.* **2018**, *120*, 016801.
(36) Zhang, C.; Zhang, Y.; Yuan, X.; Lu, S.; Zhang, J.; Narayan, A.; Liu, Y.; Zhang, H.; Ni, Z.; Liu, R.; Choi, E. S.; Suslov, A.; Sanvito, S.; Pi, L.; Lu, H.-Z.; Potter, A. C.; Xiu, F. Quantum Hall effect based on Weyl orbits in Cd_3As_2. *Nature* **2019**, *565*, 331−336.
(37) Lin, B.-C.; Wang, S.; Wiedmann, S.; Lu, J.-M.; Zheng, W.-Z.; Yu, D.; Liao, Z.-M. Observation of an oddinteger quantum Hall effect from topological surface states in Cd_3As_2. *Phys. Rev. Lett.* **2019**, *122*, 036602.
(38) Nishihaya, S.; Uchida, M.; Nakazawa, Y.; Kriener, M.; Taguchi, Y.; Kawasaki, M. Intrinsic coupling between spatially-separated surface fermi-arcs in Weyl orbit quantum Hall states. *Nat. Commun.* **2021**, *12*, 2572.
(39) Klitzing, K. v.; Dorda, G.; Pepper, M. New method for high-accuracy determination of the fine-structure constant based on quantized Hall resistance. *Phys. Rev. Lett.* **1980**, *45*, 494−497.
(40) Prange, R. E., Girvin, S. M., Eds. *The Quantum Hall Effect*, 2nd ed.; Springer New York: New York, 1990.
(41) von Klitzing, K.; Chakraborty, T.; Kim, P.; Madhavan, V.; Dai, X.; McIver, J.; Tokura, Y.; Savary, L.; Smirnova, D.; Rey, A. M.; Felser, C.; Gooth, J.; Qi, X. 40 years of the quantum Hall effect. *Nature Reviews Physics* **2020**, *2*, 397−401.
(42) Datta, S. *Electronic Transport in Mesoscopic Systems*; Cambridge University Press: Cambridge, 1995.
(43) Datta, S. *Quantum Transport: Atom to Transistor*; Cambridge University Press: Cambridge, 2005.
(44) Fisher, D. S.; Lee, P. A. Relation between conductivity and transmission matrix. *Phys. Rev. B* **1981**, *23*, 6851−6854.
(45) Jiang, H.; Wang, L.; feng Sun, Q.; Xie, X. C. Numerical study of the topological anderson insulator in HgTe/CdTe quantum wells. *Phys. Rev. B* **2009**, *80*, 165316.
(46) Groth, C. W.; Wimmer, M.; Akhmerov, A. R.; Waintal, X. Kwant: a software package for quantum transport. *New J. Phys.* **2014**, *16*, 063065.
(47) Okugawa, R.; Murakami, S. Dispersion of fermi arcs in Weyl semimetals and their evolutions to Dirac cones. *Phys. Rev. B* **2014**, *89*, 235315.
(48) Zhang, S.-B.; Lu, H.-Z.; Shen, S.-Q. Linear magnetoconductivity in an intrinsic topological Weyl semimetal. *New J. Phys.* **2016**, *18*, 053039.
(49) Borchmann, J.; Pereg-Barnea, T. Quantum oscillations in Weyl semimetals: A surface theory approach. *Phys. Rev. B* **2017**, *96*, 125153.
(50) Wu, L.; Patankar, S.; Morimoto, T.; Nair, N. L.; Thewalt, E.; Little, A.; Analytis, J. G.; Moore, J. E.; Orenstein, J. Giant anisotropic nonlinear optical response in transition metal monopnictide Weyl semimetals. *Nat. Phys.* **2017**, *13*, 350−355.
(51) Shi, L.-k.; Song, J. C. W. Large optical conductivity of Dirac semimetal Fermi arc surface states. *Phys. Rev. B* **2017**, *96*, 081410.
(52) Thouless, D. J.; Kohmoto, M.; Nightingale, M. P.; den Nijs, M. Quantized Hall conductance in a two-dimensional periodic potential. *Phys. Rev. Lett.* **1982**, *49*, 405−408.
(53) Kohmoto, M. Topological invariant and the quantization of the Hall conductance. *Ann. Phys.* **1985**, *160*, 343−354.
(54) Avron, J. E.; Seiler, R.; Simon, B. Homotopy and quantization in condensed matter physics. *Phys. Rev. Lett.* **1983**, *51*, 51−53.
(55) Halperin, B. I. Possible states for a three-dimensional electron gas in a strong magnetic field. *Jpn. J. Appl. Phys.* **1987**, *26*, 1913.
(56) Montambaux, G.; Kohmoto, M. Quantized Hall effect in three dimensions. *Phys. Rev. B* **1990**, *41*, 11417−11421.
(57) Tang, F.; Ren, Y.; Wang, P.; Zhong, R.; Schneeloch, J.; Yang, S. A.; Yang, K.; Lee, P. A.; Gu, G.; Qiao, Z.; Zhang, L. Three-dimensional quantum Hall effect and metal−insulator transition in $ZrTe_5$. *Nature* **2019**, *569*, 537−541.
(58) Qin, F.; Li, S.; Du, Z.; Wang, C.; Zhang, W.; Yu, D.; Lu, H.-Z.; Xie, X. Theory for the charge-density-wave mechanism of 3D quantum Hall effect. *Phys. Rev. Lett.* **2020**, *125*, 206601.
(59) Galeski, S.; Ehmcke, T.; Wawrzyńczak, R.; Lozano, P. M.; Cho, K.; Sharma, A.; Das, S.; Küster, F.; Sessi, P.; Brando, M.; Küchler, R.; Markou, A.; Köonig, M.; Swekis, P.; Felser, C.; Sassa, Y.; Li, Q.; Gu, G.; Zimmermann, M. V.; Ivashko, O.; Gorbunov, D. I.; Zherlitsyn, S.; Förster, T.; Parkin, S. S. P.; Wosnitza, J.; Meng, T.; Gooth, J. Origin of the quasi-quantized Hall effect in $ZrTe_5$. *Nat. Commun.* **2021**, *12*, 3197.
(60) Weiße, A.; Wellein, G.; Alvermann, A.; Fehske, H. The kernel polynomial method. *Rev. Mod. Phys.* **2006**, *78*, 275−306.
(61) García, J. H.; Covaci, L.; Rappoport, T. G. Rappoport, Real-space calculation of the conductivity tensor for disordered topological matter. *Phys. Rev. Lett.* **2015**, *114*, 116602.
(62) Fan, Z.; Garcia, J. H.; Cummings, A. W.; Barrios-Vargas, J. E.; Panhans, M.; Harju, A.; Ortmann, F.; Roche, S. Linear scaling quantum transport methodologies. *Phys. Rep.* **2021**, *903*, 1−69.

https://doi.org/10.1021/acs.nanolett.2c00296
Nano Lett. 2022, 22, 3033−3039